



HAL
open science

On the potential of ultrasonic time of flight instrumentation for the monitoring of thermal phenomena in Laser Powder Bed Fusion

Marie Palla, Florian Le Bourdais, Jean-Paul Garandet

► To cite this version:

Marie Palla, Florian Le Bourdais, Jean-Paul Garandet. On the potential of ultrasonic time of flight instrumentation for the monitoring of thermal phenomena in Laser Powder Bed Fusion. *AIP Advances*, 2024, 14 (8), pp.085205. 10.1063/5.0203520 . cea-04784247

HAL Id: cea-04784247

<https://cea.hal.science/cea-04784247v1>

Submitted on 14 Nov 2024

HAL is a multi-disciplinary open access archive for the deposit and dissemination of scientific research documents, whether they are published or not. The documents may come from teaching and research institutions in France or abroad, or from public or private research centers.

L'archive ouverte pluridisciplinaire **HAL**, est destinée au dépôt et à la diffusion de documents scientifiques de niveau recherche, publiés ou non, émanant des établissements d'enseignement et de recherche français ou étrangers, des laboratoires publics ou privés.

RESEARCH ARTICLE | AUGUST 02 2024

On the potential of ultrasonic time of flight instrumentation for the monitoring of thermal phenomena in laser powder bed fusion

M. Palla ; F. Le Bourdais ; J. P. Garandet 

AIP Advances 14, 085205 (2024)

<https://doi.org/10.1063/5.0203520>

Articles You May Be Interested In

Machine learning-powered lead-free piezoelectric nanoparticle-based deep brain stimulation: A paradigm shift in Parkinson's disease diagnosis and evaluation

AIP Advances (March 2024)

Temporal factors in referential intensity coding

J Acoust Soc Am (August 1996)

Ultrasound characterization of bioinspired functionally graded soft-to-hard composites: Experiment and modeling

J. Acoust. Soc. Am. (March 2022)



Special Topics Open for Submissions

[Learn More](#)

On the potential of ultrasonic time of flight instrumentation for the monitoring of thermal phenomena in laser powder bed fusion

Cite as: AIP Advances 14, 085205 (2024); doi: 10.1063/5.0203520

Submitted: 14 June 2024 • Accepted: 12 July 2024 •

Published Online: 2 August 2024



View Online



Export Citation



CrossMark

M. Palla,^{1,a)}  F. Le Bourdais,^{1,b)}  and J. P. Garandet² 

AFFILIATIONS

¹ Université Paris-Saclay, CEA LIST, 91191 Gif-sur-Yvette, France

² Université Grenoble Alpes, CEA LITEN, 38000 Grenoble, France

^{a)} Author to whom correspondence should be addressed: marie.palla.sollin@gmail.com

^{b)} Email: florian.lebourdais@cea.fr

ABSTRACT

The present paper describes a proof of concept showing the ability of ultrasound time of flight measurements to complement existing temperature measurements in a laser powder bed fusion additive manufacturing process. To this end, two printers (a 3D Systems ProX DMP 320 and a Farsoon FS 271M) were instrumented with ultrasonic transducers, as well as with thermal cameras and thermocouples. The obtained results show that the time of flight signals can provide information that is both consistent and complementary with the data from the standard thermal camera and thermocouple systems. Such a conclusion is shown to be valid at both the macroscopic (i.e., whole fabrication) and the microscopic (individual layer melting and solidification) time scales. The present work shows that ultrasound time of flight data are a useful *in situ* diagnostic measurement. In addition, we discuss how it could be used for the validation of layer scale numerical models of the thermal phenomena during the printing process.

© 2024 Author(s). All article content, except where otherwise noted, is licensed under a Creative Commons Attribution-NonCommercial-NoDerivs 4.0 International (CC BY-NC-ND) license (<https://creativecommons.org/licenses/by-nc-nd/4.0/>). <https://doi.org/10.1063/5.0203520>

I. INTRODUCTION

Since its first steps in the 1980s, additive manufacturing continues to expand and has great prospects in many industry sectors, especially aeronautics, space, medical, or automotive (Giannatsis and Dedoussis, 2009; Uriondo *et al.*, 2015). Different manufacturing techniques have been developed for various types of materials (Gawel, 2020), but for metallic alloys, the technique consisting in selective layer-by-layer melting of a deposited powder bed by a laser, referred to as Laser Powder Bed Fusion (LPBF), currently seems the most advantageous for the production of complex and high quality metal parts. As in all processes allowing for the elaboration of a solid part from a liquid phase, temperature is a key process variable in LPBF, as it controls powder melting, melt pool solidification, and the formation of the parts microstructure (DebRoy *et al.*, 2018).

In this context, it was quite natural that a number of previous works aimed at the determination of some temperature characteristics of the process for monitoring purposes. As IR sensors, e.g., pyrometers or thermal cameras, can be used with relative ease within

an LPBF fabrication chamber, a number of interesting results (see, e.g., Bartlett *et al.*, 2018; Mitchell *et al.*, 2020; and Yan *et al.*, 2018) have thus been obtained, often with the objective of assessing the presence of metallurgical defects. However, IR sensors can only probe the top of the growing part, but do not give direct access to the internal temperature field. Other measurement techniques exist, either classical, such as the use of thermocouples (TC), or quite original, such as the embedding of Bragg-fiber gratings into the build for temperature measurement (Lerner *et al.*, 2022), but it can be safely stated that the problem of *in situ* part temperature measurement in LPBF remains a challenge.

To provide complementary insights on this complex issue, one could consider using information from ultrasonic (US) wave propagation. Indeed, ultrasound waves have the particularity that their velocity is sensitive to the temperature of the propagating medium. This sensitivity has been used in various applications, e.g., in air and in solid waveguides based on time of flight measurement in the pulse echo mode (Ihara *et al.*, 2013; Liang *et al.*, 2017; and Wang *et al.*, 2018). More specifically, assuming that the ultrasound

velocity is constant in the direction normal to propagation, the quantity

$$t_L = 2 \int_0^L \frac{dz}{v(z)} = 2 \int_0^L \frac{dz}{v(z, T(z))} \quad (1)$$

is the time of flight measured between an emission transducer and a suitable echo situated at a distance L from the source. As such, considering that the velocity at a location z depends on temperature, the time of flight will depend on the thermal field along the wave propagation path. It should be noted that this is of course an approximation since the local velocity also depends on the stress state, the presence of defects, such as porosities, and other parameters. However, we choose to neglect effects other than temperature as a first-order approximation, as other authors have done. Provided a suitable inversion procedure can be implemented using appropriate initial conditions, the whole temperature field within the part can be reconstructed (Ihara *et al.*, 2013; Shi *et al.*, 2020). To do so, an analytic expression relating wave velocity and temperature is necessary. Such a relation may be quite complex to obtain, but a linear relation of the form $v(T) = -aT + b$ can often be used over a limited temperature range (Chen *et al.*, 1999; Wadley *et al.*, 1986), with values for the a coefficient typically in the $1 \text{ m s}^{-1} \text{ K}^{-1}$ range.

Even though not obvious due to technical reasons we will discuss in detail further on, it should be stated that a number of authors already implemented ultrasonic techniques within LPBF machines. For instance, Kouprianoff *et al.* demonstrated the potential of the acoustic emission technique for the online monitoring of defect formation (Kouprianoff *et al.*, 2021). Closer to our present purposes, the possibility of using the ultrasonic pulse-echo mode for time of flight measurement was demonstrated by Rieder *et al.* (2014; 2016). These authors placed an ultrasonic transducer underneath the build plate and recorded ultrasound signals during the build of a cylinder with the aim to detect intentionally manufactured internal defects. With the transducer in place, they varied laser power to generate defects and monitored the quality of the part based on the recorded scans.

When the sample was devoid of internal defects generating spurious echoes, Rieder *et al.* were able to show that the measured time of flight depended on the location L [see Eq. (1)] at the top of the growing part. Indeed, due to repeated powder deposition, melting, and solidification, L will be an increasing function of the build time. The Ph.D. thesis work of Nadimpalli (2018) was built upon the observations of Rieder and investigated the use of the layer by layer interfacial stiffness model, allowing us to describe the quality of each layer and fitting it to the data collected using ultrasound. However, he did not investigate the dynamic nature of the signals he recorded.

In addition, very interesting in relation to our present purposes is the recent work of Raffestin *et al.* (2023) that used a pulse-echo configuration to demonstrate that the melted layer thickness could vary by as much as $\pm 30\%$ along fabrication, as such variations can have a significant impact on local heat transfer phenomena.

In this context, our purpose in the present work is to propose a proof of concept of the ability of ultrasound propagation characteristics to complement existing standard temperature measurements in a laser powder bed fusion additive manufacturing process. In practice, we use an experimental setup similar to that of Rieder *et al.* and show that the analysis of the time of flight signals

allows us to obtain relevant information at both the macroscopic (i.e., whole fabrication) and the microscopic (individual layer melting and solidification) time scales that is consistent with additional data that were collected using thermocouples and infrared cameras. In order to support the robustness of the implemented technique, measurements were conducted in two different machine setups, using materials with significantly different thermal properties, namely, an Inconel and an aluminum-based alloy.

More precisely, Sec. II details the experimental system developed, as well as the machines and manufacturing specificities. It also presents the *a posteriori* ultrasound velocity measurements carried out and dwells in detail on the signal processing carried out on the various data recorded. The results from ultrasonic time of flight measurements at the fabrication scale are then presented in Sec. III and discussed in connection with the IR and thermocouple data. A similar approach is proposed in Sec. IV for the signals obtained at the individual layer scale, with a special emphasis on the possibility of extracting characteristic decay time when the laser is switched off. Finally, concluding remarks and perspectives are proposed in Sec. IV.

II. MATERIALS AND METHODS

A. Ultrasonic and thermal instrumentation

A schematic of a typical LPBF setup is shown in Fig. 1. The measurement technique used by Rieder *et al.* (2014; 2016) consists in fixing an ultrasonic transducer underneath a specially purposed fabrication plate below the part to be built, as seen in Fig. 1. For our experiments, we chose a Panametrics probe resonating at 5 MHz, with an acoustic diameter of 25 mm that generates longitudinal waves. The transmission of the waves in the plate was ensured by a Sofranel shear-type couplant. A 5072PR-Olympus pulser-receiver controlled the emission and the reception of the ultrasonic pulses. An analog high-pass filter of 1 MHz was applied to the received signals, which were then digitized by using a PicoScope 6402D controlled by a PC. Additional thermal monitoring instruments were also installed in the machine to gather temperature variations at different locations. Two thermocouples of type K were attached underside the build platform, near the transducer (more on this below). The acquisition was realized with a multichannel data logger Novus FieldLogger, which recorded two temperature values per second, with a digital accuracy set to $0.1 \text{ }^\circ\text{C}$.

We first instrumented a 3D Systems ProX DMP 320 printer to manufacture two cylinders denoted as Builds 1A and 1B. The setup described above was installed in this machine. Magnets fixed the transducer and the thermocouples underneath the steel build plate, as seen in Fig. 2(a). For the first build, the thermocouples were placed at distances of 2 and 4.4 cm from the transducer, and for the second build, the thermocouples were placed at distances of 2.1 and 4.1 cm from the transducer. A FLIR thermal camera was placed inside the build-chamber to record the temperature at the sample surface using a mirror to avoid direct laser exposure; see Fig. 2(b). The recording framerate was 10 Hz, allowing an average of 258 images per layer fabrication (more on that below). Additionally, a Thorlabs PDA100A2 photodiode was fixed next to the camera, to capture the light level inside the build chamber and thus accurately determine the duration of the lasing phases. Figure 2(b) shows the final setup. The recoater and the build plate were specially adapted to let the

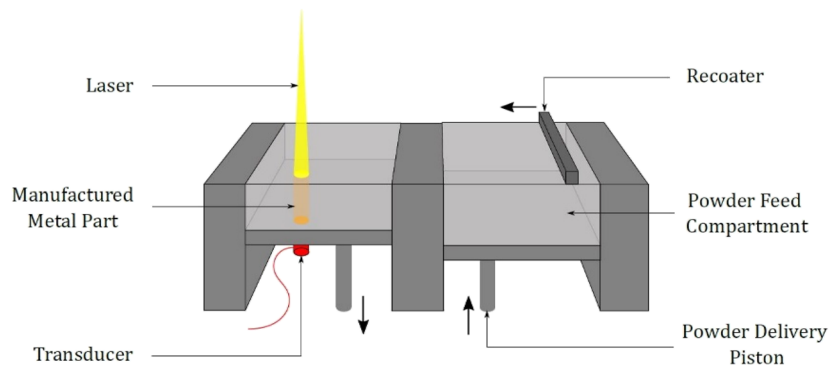


FIG. 1. Schematic of the LPBF machine and ultrasonic probe location underneath the build plate.

wires of the instruments pass into the build-chamber. The PicoScope acquired ultrasonic signals that were sampled at 52 MHz and with a repetition frequency of 10 Hz, i.e., to record one signal each 0.1 s. It simultaneously acquired the photodiode data at the same rate. For reasons that are not fully clear at this point, but that could be related to couplant aging in the machine environment or to energy dissipation associated with the fine grain crystallographic structure common in LPBF materials, the signal amplitude was found to decrease along fabrication. It was thus decided to increase the gain, respectively, by 20 dB after 1 h 20 min of manufacturing for Build 1A and by 15 dB after 1 h of manufacturing for Build 1B.

Similarly, we instrumented a Farsoon FS271M printer to manufacture another cylinder, denoted as Build 2. Aluminum tape was used to hold the transducer underneath the aluminum build plate. The thermocouples were attached with Kapton tape, one in contact with the transducer and the second at the center of the plate, about 92 mm from the transducer, as seen in Fig. 3(a). Their installation required dismantling the plate and passing the cables of the various sensors through a hole generally used for the resistor of the heating plate, which was removed during this experiment. A thermal camera Optris PI 640i G7 observed the sample surface through a germanium optical window from above the build chamber. It was

installed on a support specially designed so that it was slightly tilted at an angle to be aligned with the surface of the cylinder, as seen in Fig. 3(b). The recording framerate was set to 10 Hz, allowing an average of 180 images per layer fabrication. For this build, no photodiode was available. As in the 3D Systems setup, the signal amplitude was found to decrease along fabrication, so 9 dB of gain was added after 1 h 40 min of manufacturing. The ultrasonic signal acquisition was improved compared to the ProX DMP setup by increasing the sampling and pulse repetition frequencies to 156 MHz and 300 Hz, respectively, and by implementing a moving average procedure on each set of 20 time of flights. Therefore, 15 signals per second are recorded for Build 2.

B. Materials and manufacturing characteristics

An Inconel 625 powder was used in the 3D Systems ProX DMP 320 printer from the Additive Factory Hub platform. The LaserForm Ni625 powder provided by the machine manufacturer used for these builds had values of the D10, D50, and D90 volume percentiles of, respectively, 19.2, 32.8, and 51 μm . Build 1A was a cylinder 25 mm in diameter and 100 mm in height. It was built in 1733 layers, with the whole fabrication lasting 12 h 20 min. Build 1B was a cylinder

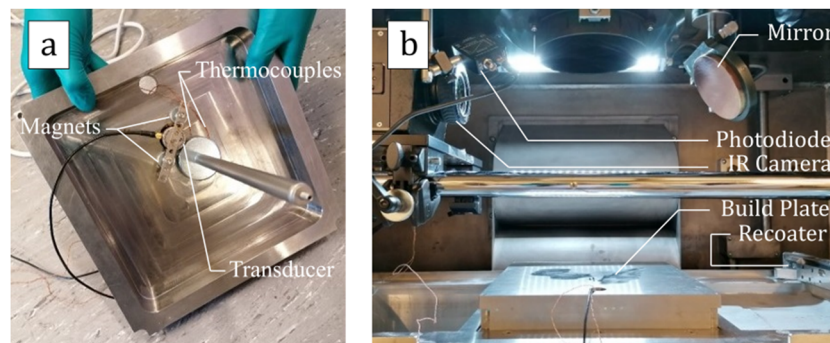


FIG. 2. Setup installation in the ProX machine: (a) Transducer and two thermocouples held by magnets underneath the build plate and (b) build plate, thermal camera, and photodiode positions inside the build chamber.

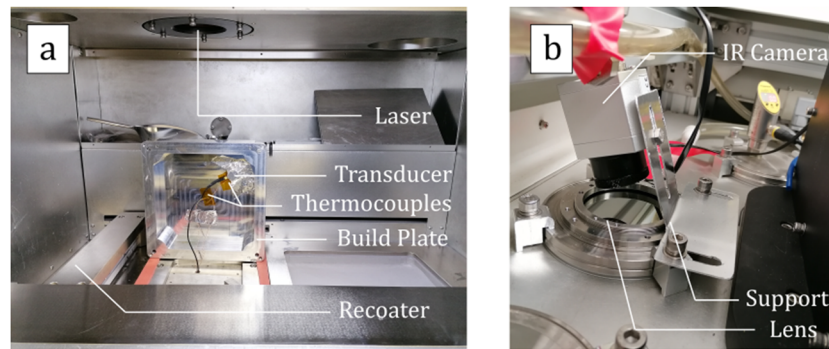


FIG. 3. Instrumentation of the Farsoon machine: (a) transducer and thermocouples fixed underneath the build plate and placement in the machine and (b) infrared camera placed above the build-chamber.

TABLE I. ProX process parameters for Builds 1A and 1B.

Parameters	Values
Power laser (W)	254
Hatch spacing (μm)	100
Scan speed (mm/s)	900
Laser spot diameter (μm)	60
Powder layer thickness (μm)	60

15 mm in diameter and 50 mm in height, made of 916 layers, with a fabrication duration of 6 h 40 min. [Table I](#) shows the process parameters for these two builds. These parameters have been selected to ensure that Builds 1A and 1B reach $\sim 100\%$ density compared to bulk Inconel. In the 3D Systems ProX DMP 320 printer, the fabrication plate was made of tool steel. In order to avoid stress concentrations and to ensure a smooth transition between the builds and the fabrication plate, the diameter of the first 65 layers was slightly higher than that of the cylinders, with a scan velocity of 2000 mm/s. With such a high scan velocity, a certain level of porosity can be expected in those layers, which is favorable in terms of stress decoupling.

In a different series of experiments, an aluminum AlSi7Mg0.6 powder was used in the Farsoon FS271M printer to build a cylinder of 20 mm diameter and 15 mm in height, composed of 494 layers, which took 2 h 30 min to produce. The powder was provided by Toyal, and the values of the D10, D50, and D90 volume percentiles were, respectively, of 27, 40, and 59.5 μm . [Table II](#) summarizes the

TABLE II. Farsoon process parameters for Build 2.

Parameters	Values
Power laser (W)	200
Hatch spacing (μm)	170
Scan speed (mm/s)	1000
Laser spot diameter (μm)	130
Powder layer thickness (μm)	30

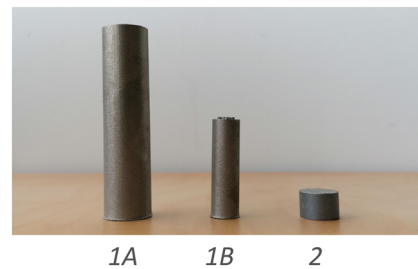


FIG. 4. Image showing the cylinders manufactured in the ProX machine (1A, 1B, Inconel) and Farsoon machine (2, aluminum).

process parameters used; these parameters were selected based on previous experience to provide full density samples when activating the heating plate. As mentioned above, the heating system had to be removed to allow for the implementation of the US instrumentation. Altogether, this resulted in a porosity in the Build 2 sample of the order of 5%. In the Farsoon FS271M printer, the fabrication plate was made of a 6000 series aluminum alloy, which can be considered close, in terms of both thermal and mechanical properties, to the fabricated AlSi7Mg0.6 grade.

The built cylinders are shown side by side in [Fig. 4](#).

The setups described in the previous paragraphs allowed for the acquisition of datasets for each build, and we now have to turn to the very important issue of signal processing, which will be discussed in some detail in [Sec. II C](#).

C. Signal processing of acquired datasets and time of flight measurement

The datasets of the builds described above consisted of ultrasound signals, thermal camera images, thermocouple temperatures, and photodiode signals (Builds 1A and 1B only). Starting with the processing of the ultrasound signals, which represent the most original contribution of the present work, a review of the various techniques allowing for the measurement of time of flights (TOF) can be found in the work of [Svilainis \(2013\)](#). Before going into more details, it is worth taking a qualitative look at the raw signals

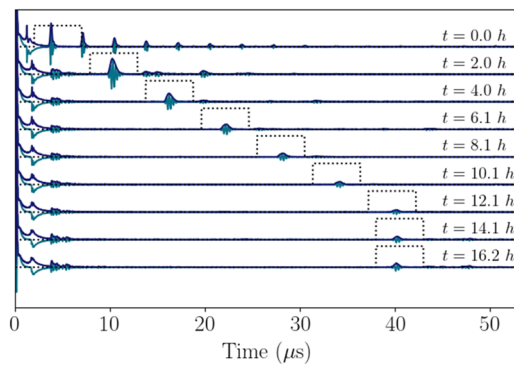


FIG. 5. Ultrasonic signals recorded during Build 1A and their envelopes calculated with the Hilbert transform.

represented in Fig. 5 for Build 1A. The first line at $t = 0.0$ h is the result of an acquisition carried out prior to the beginning of the construction of the cylinder, i.e., when the time of flight echoes are due to the upper and lower parts of the fabrication plate. It can be seen that the quality of the signal is good, with numerous echoes detectable, due to back and forth reflections in the build plate. As time increases, the first echo remains at a fixed position, characteristic of the interface between fabrication plate and cylinder, since the acoustic impedances of tool steel and Inconel are slightly different.

Also visible in Fig. 5 are shifting echoes that can be attributed to a reflection from the top surface of the growing cylinder. However, as opposed to the situation at $t = 0.0$ h, the number of visible echoes is much reduced, with a barely detectable second echo on the $t = 2.0$ h line and none afterward. In our opinion, this can be attributed to strong dissipation of the ultrasound energy in the fabricated part, which in turn can be explained by the fine grain crystallographic structure common in LPBF fabricated materials as mentioned above. In practice, this means that the time of flight measurements will have to be taken between the initial pulse and the only remaining echo. In practice, this means that the time necessary for signal propagation within the couplant, which cancels when measurements are taken between echoes, will have to be taken into account, a point that will be discussed further below.

Back to the determination of time of flights, we decided to test techniques based on the determination of the maximum of the signal, the maximum of its envelope, and the time location of the crossing of the ordinate axis (zero crossing method). We thought about implementing the widely used cross-correlation technique, which is based on the calculation of the cross-correlation function

between the received signal and a reference signal. However, in our measurements, we observed that the shape of the received signal is slightly modified during the manufacturing, and in such a case, the cross-correlation method is less effective (Svilainis, 2013).

Sampling frequency being often an issue, interpolation methods have been developed to increase the accuracy of the time of flight measurements on subsampled signals (Svilainis, 2019; Boucher and Hassab, 1981; and Carter, 1985). In the present work, several interpolation functions were investigated, which yielded very similar results. We thus decided to work on either linear (for the zero crossing) or parabolic (for the signal and envelope maxima) fits, which are simple to use and computationally efficient. With our 52 MHz sampling frequency for Builds 1A and 1B, the number of fitting points was set to 15, whereas with the 156 MHz sampling frequency used for Build 2, 30 fitting points were used.

These various techniques were tested *in situ* but prior to fabrication, i.e., when the time of flight echoes are due to the upper and lower parts of the fabrication plate. Table III shows the ultrasound velocities deduced from the time of flight measurements for Build 1A using the time difference between the first echo and the initial pulse, the time difference between the second and first echoes, or the time difference between the third and second echoes.

The first thing to be noticed is that for a given measurement procedure, all techniques yield very similar results, the discrepancies remaining in the 1% range, which appears more than satisfying for a proof of concept type of work. In addition, in absolute terms, the deduced values measured between the first and second or the second and third echoes are close to 6000 m/s and thus in full agreement with typical ultrasound velocities in bulk tool steel. On the other hand, quite significant differences (of more than 10%) are observed when the velocity measurements are based on the difference between the initial pulse and the first echo.

As mentioned earlier, these apparently lower velocities can be associated with the time lag due to the ultrasound propagation within the couplant, which cancels when the measurement is carried out between echoes. An accurate determination of the couplant thickness is outside the scope of the present work, but taking a reasonable value of ultrasound velocity within the couplant of 1500 m/s, the thickness required to recover the values measured between echoes is of 340 μm , which is certainly a good order of magnitude estimate. Allowing the ultrasound velocity within the couplant to increase between 1300 and 1700 m/s, the associated thicknesses would vary between 310 and 410 μm , thus remaining within physically sound ranges.

Regarding the difference of measured velocities between various measurement techniques, similar results were obtained on Builds 1B and 2, with nearly identical results. In quantitative terms,

TABLE III. Various determinations of ultrasonic velocities in tool steel from time of flight measurements for Build 1A. All values are in meters per second.

	Signal maximum	Envelope maximum	Zero-crossing	Signal maximum, parabolic fit	Envelope maximum, parabolic fit	Zero-crossing, linear fit
First echo	5257	5311	5311	5251	5298	5319
First and second echoes	6017	5982	6052	6022	5998	6030
Second and third echoes	6017	5982	6017	6024	5997	6030

the deduced values for ultrasound velocity measured between the first or second or the second and third echoes are again very close to expected values: 6000 m/s for Build 1B (that is within 1% of what had been obtained on Build 1A) and 6500 m/s, typical of aluminum type alloys, for Build 2. In addition, on both Builds 1B and 2, quite significant differences (of the order of 10%) are again observed when the velocity measurements are based on the difference between the initial pulse and the first echo.

The couplant thicknesses necessary to recover the expected ultrasound velocities in Builds 1B and 2, respectively, in tool steel and in aluminum, are also found to be nearly identical (say within $\pm 5 \mu\text{m}$) to the $340 \mu\text{m}$ deduced for Build 1A. Such a coincidence could not have been *a priori* expected, but it is reassuring to see that the couplant thickness values are expected to be similar between various experiments. As there is no guarantee that couplant characteristics (thickness and ultrasound velocity) will remain the same all along fabrication, we did not attempt to correct the measured time of flights from the bias due to couplant time lag.

We emphasize that doing pulse-echo time of flight measurements based on a single echo is not common (even discouraged) practice, but in our situation, we did not have any other option. Fortunately, since in the following we will mostly focus on their variations, the absolute values of the time of flight will not matter so much. Had we targeted quantitative analysis (see perspectives), a better method would be needed. Back to Table III, in view of the small but significant discrepancies observed between the various measurement techniques, we decided to ascribe an absolute uncertainty of 100 m/s on all velocity measurements. Incidentally, such a 100 m/s uncertainty value was also proposed by Raffestin *et al.* (2023) in their similar experimental configuration.

Since a choice had to be made between measurement techniques, we decided to implement the method based on the maximum envelope estimate with fitting as detailed below. First, the envelope of each ultrasonic signal is calculated using the Hilbert transform. This is shown in dark blue in Fig. 5, with signals sampled at constant time intervals from the full build data. A moving rectangular window, corresponding to the dotted lines, allowed for extracting the echo of interest. The window was set to move in a manner correlated with the fabricated cylinder height. A parabolic

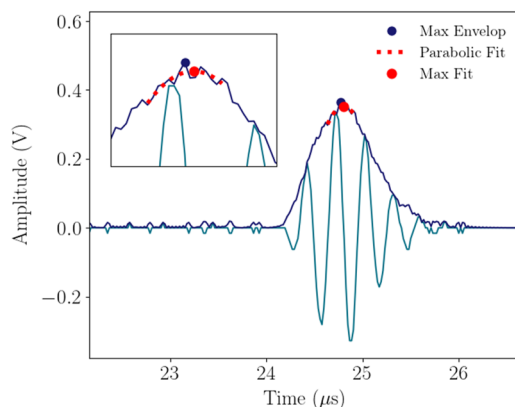


FIG. 6. Time of flight extraction with envelope calculation by Hilbert transform. Inset: Zoom on the fit maximum.

fit is then realized near the envelope maximum. The time of flight is finally taken to be the maximum of this parabolic fit, represented by the red point in Fig. 6. These operations were realized on all acquired ultrasonic signals, allowing for the observation of the evolution of the time of flight during the manufacturing process for all builds.

As for the thermal cameras, their images were processed with their respective manufacturer infrared thermography analysis software. We selected a circular region of interest (ROI) centered on the cylinder surface and extracted the average temperature in this ROI. Thus, one value of temperature per image of the sample surface was recorded, corresponding to an average of 258 temperature values per layer fabrication for Builds 1A and 1B and an average of 180 temperature values per layer fabrication for Build 2. It is important to state that absolute temperature measurements by using an infrared camera require difficult evaluation of the material emissivity, among other parameters, which can also vary along fabrication (Bartlett *et al.*, 2018) and that our cameras are not expected to provide reliable data below 100°C .

In the absence of an in-depth calibration procedure, the absolute temperature values that will be presented further on should be taken with caution. The issue of inferring a true temperature from an IR signal is especially true for Build 2, where the thermal camera is placed behind a germanium window, which could have a significant effect on absolute temperature measurements. Still, an IR camera signal remains valuable information to study temperature variations, especially during the cooling phases of the part, and our opinion is that it can be used for order of magnitude interpretation of the data.

In the same way, absolute temperature measurements obtained from thermocouples should be interpreted with caution due to possible effects such as solder oxidation or the reliability of the thermocouple attachment to the fabrication plate. It can also be noted that these effects can vary from one experiment to another and even during the course of a single fabrication run. Nevertheless, when compared to thermal camera data, thermocouples can be considered a more reliable data source in terms of absolute temperature measurements.

The photodiode signal implemented in Builds 1A and 1B takes the form of a noisy irregular square wave, which was maximal during the times for which the laser is active. A maximum filter was applied on a sliding window, and a simple thresholding allowed identifying the time stamps corresponding to the “laser on” and “laser off” events. Since we had no photodiode for Build 2, the camera signal was used instead to extract the lasing times. Therefore, for Build 2, we applied a maximum filter followed by a minimum filter over the sliding window to extract and remove the baseline from the signal. Since the clocks of the various acquisition systems were not initially synchronized, the thermocouples and camera data were interpolated on the acquisition time of ultrasonic signals and time-adjusted.

D. Post-fabrication velocity measurements

The final procedure step before turning to the actual presentation of the obtained results was to *a posteriori* measure the ultrasound velocities in the fabricated samples. After completion of the experiments, the three cylinders were separated from their respective build plates and submitted to pulse echo measurements in a thermal enclosure. More details on the procedure and specially the

care to ensure that thermal equilibrium was actually attained can be found in Marie Palla's thesis (Palla, 2023). Various signal-processing techniques were again tested, but for the sake of consistency with Sec. II C, we decided to stick with the maximum envelope estimate with fitting. The results for Builds 1A and 1B are as follows:

$$v_{1A}(\text{m/s}) = -0.48T(^{\circ}\text{C}) + 5739, \quad (2a)$$

$$v_{1B}(\text{m/s}) = -0.66T(^{\circ}\text{C}) + 5852. \quad (2b)$$

The first thing to be noted is that in absolute terms, the measured values are close but somewhat smaller to what can be expected for a standard wrought Inconel 625 alloy. However, as noted by Kumar *et al.* (2002), the material structure can have a significant influence on propagation velocity, and the grain size in our additively manufactured samples can be expected to be much smaller as compared to wrought materials. A similar argument can be invoked to account for the slight differences observed between Builds 1A and 1B. Indeed, even though those samples were fabricated on the same machine using the same process parameters, the heat transfer phenomena, and thus the solidification structure, can be expected to be somewhat different due to the various sample sizes.

In principle, it could be argued that more work would be necessary to shed some light on the observed differences and to accurately assess the velocity–temperature relationship of our additively manufactured material, as done, e.g., by Javidrad and Salemi (2020). All the same, since the observed differences remain within the 100 m/s uncertainty bar, our opinion is that the above relationships can be used for a proof of concept type of study. Regarding the AlSi7Mg0.6 of Build 2, the identified velocity temperature relationship takes the following form:

$$v_2(\text{m/s}) = -1.34T(^{\circ}\text{C}) + 5364. \quad (3)$$

The temperature coefficient appears to be significantly higher as compared to the Inconel 625 alloys, but remains within the $1 \text{ m s}^{-1} \text{ K}^{-1}$ range identified in the literature. However, what appears significant are the quite low absolute velocities observed since US velocities in aluminum-based alloys are expected to be around 6500 m/s; cf. also our own measurement on the fabrication plate in Sec. II C. Our opinion is that the low velocities observed are related to the porosity of the Build 2 sample. It may appear

a priori surprising that a limited 5% porosity should result in a circa 20% velocity reduction, but this is not inconsistent with literature data (Slotwinski *et al.*, 2014).

III. RESULTS AND DISCUSSION

A. Time of flight data at fabrication scale

Applying the previously detailed procedure, Fig. 7 represents the various recordings of US data for the full duration of Builds 1A, 1B, and 2. The first thing to be noted is that, apart from deviations in the initial and final stages of Builds 1A and 1B, the time of flight appears linear when plotted against fabrication time. Such an evolution is to the first order consistent with the construction of the cylinders, whose height increases by a similar amount with each additional layer. Such a linear behavior has also been observed on the scans recorded by Rieder *et al.* (2016). Indeed, as stated in the Introduction, due to the repeated powder deposition, melting, and solidification steps of the additive manufacturing process, the echo location $L(t)$ is expected to have a staircase-like evolution. At the time scale of an entire build, such staircase variations are not visible and $L(t)$, resulting in the observed linear behavior.

We will come back in some detail on the issue of whether such a linear behavior is consistent with the expected temperature variations when we present IR and thermocouple data in Sec. III B. What can be tested at this point is whether the values deduced from a simplified version of Eq. (1) are consistent with the *ex situ* values proposed in Eqs. (2a), (2b), and (3). To do so, let us assume that the US propagation within the couplant and the supporting plate remain the same all along fabrication. Then, the slope of the linear profiles in Fig. 7 can be identified with $(2/\underline{V})$ times the fabrication velocity, where \underline{V} represents the harmonic velocity of the US velocity within the part and where the fabrication velocity can be approximated by the ratio of the layer thickness to the heating/cooling cycle duration. Plugging in the experimental slopes measured in Fig. 7 and the process parameters listed in Tables I and II, one finds \underline{V} values of 5636, 5725, and 5488 m/s for Builds 1A, 1B, and 2, respectively, with again an uncertainty bar of circa 100 m/s.

The first thing to be said is that it is reassuring to find values in relatively close agreement with those proposed in Eqs. (2a), (2b), and (3). *A priori* surprising is the case of Build 2 since the deduced \underline{V} is slightly higher than the *ex situ* measured velocity at 0°C , but the discrepancy remains within reasonable bounds especially in view of the

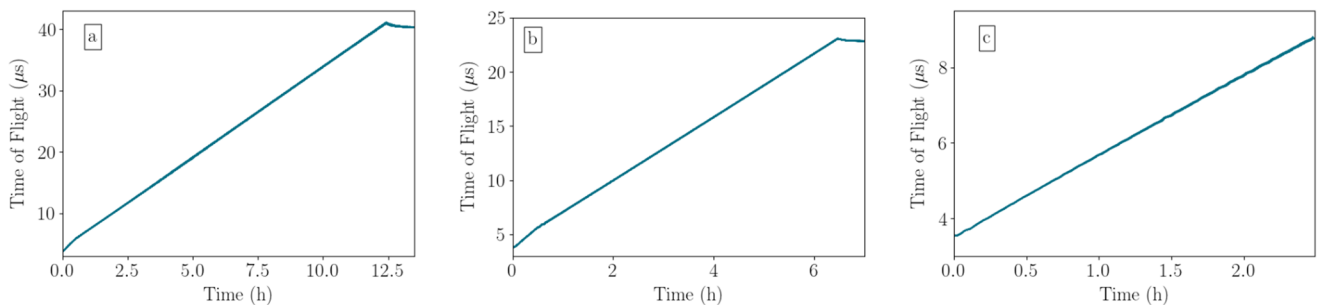


FIG. 7. TOF data for the entire duration of Builds (a) 1A, (b) 1B, and (c) 2.

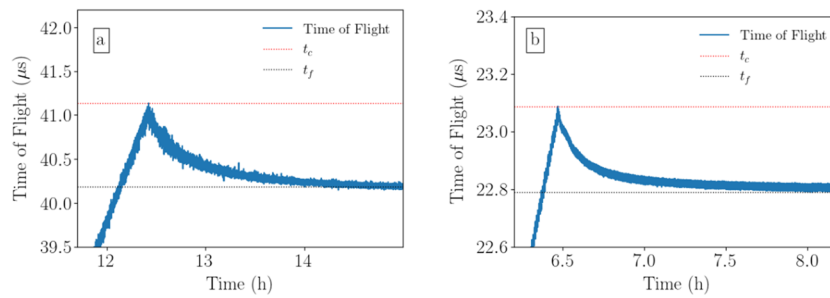


FIG. 8. Final transients after the end of fabrication: (a) Build 1A. (b) Build 1B.

100 m/s uncertainty on both measurements. As for Builds 1A and 1B, the deduced \underline{V} is lower than the *ex situ* measured velocities, it is thus tempting to see whether temperature variations could account for the observed difference. Plugging in the data from Eqs. (2a) and (2b), the average temperature along fabrication should be of the order of 215 and 192 °C in Builds 1A and 1B, respectively.

As the differences in velocity values barely exceed the uncertainty, one should be careful in drawing hasty conclusions, especially on quantitative issues, but additional evidence can be obtained from the analysis of the post-fabrication time of flights. Indeed, once the fabrication has been completed, the geometry remains fixed and the decrease in time of flights can be ascribed to a cooling of the samples. Such relaxations are presented in Fig. 8 for Builds 1A and 1B. As for Build 2, the acquisition was stopped right after the last lasing stage, so no data are available.

The measured time of flight differences between the end of fabrication and the end of acquisition due to the cooling of the cylinders are of 0.81 and 0.27 μs , respectively, for Builds 1A and 1B. Such time of flight differences can be converted in ultrasound velocity differences based on the sample length and the average US velocity. For Build 1A, plugging in $L = 100$ mm and $\underline{V} = 5636$ m/s, we find a velocity variation of 129 m/s that can be translated in a temperature relaxation during cooling of 268 °C using the temperature coefficient of Eq. (2a). For Build 1B, plugging in $L = 50$ mm and $\underline{V} = 5724$ m/s, we find a velocity variation of 88 m/s that can be translated in a temperature relaxation during cooling of 134 °C using the temperature coefficient of Eq. (2b).

Such values are of the same order of magnitudes than those measured from the slopes of the time of flight vs fabrication time, but too much emphasis should not be laid on quantitative issues. It should be first stated that what is measured from the relaxation times at the end of fabrication is the average sample temperature of the sample at this time location, whereas what is measured from the overall slopes is the average temperature during the whole fabrication. We will discuss in more detail these issues in Sec. III B after the presentation of the IR and TC data.

More significant are the very different slopes of the time of flight vs fabrication time at the beginning of Builds 1A and 1B during the fabrication of the first 65 layers. Applying the same procedure of identification of these slopes with $(2/\underline{V})$ times the fabrication velocity, the average US velocities \underline{V} are found to be of 4003 and 4281 m/s for Builds 1A and 1B, respectively. Whether these velocities can be considered as identical is questionable in view of the error bars on the measurements, but what can be clearly stated is that such low values cannot be ascribed to temperature variations, but rather to the porosity of the fabricated samples. As mentioned earlier (Slotwinski *et al.*, 2014), the issue of velocity variations vs porosity is not a simple one, but our results are not inconsistent with published data.

B. Input from IR and TC data and discussion

The data all along the fabrication are shown in Figs. 9 and 10 for the IR camera and thermocouple data, respectively. The first

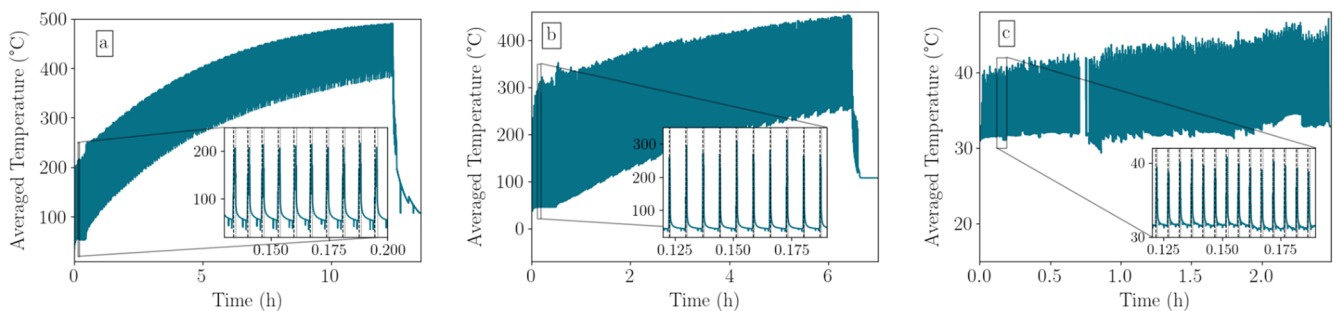


FIG. 9. IR camera data all along fabrications for Builds (a) 1A, (b) 1B, and (c) 2.

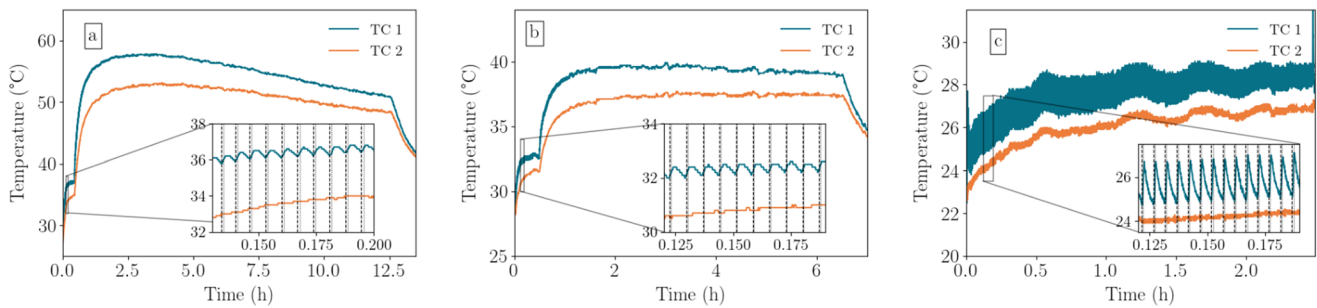


FIG. 10. Thermocouple data all along fabrications for Builds (a) 1A, (b) 1B, and (c) 2.

thing to be noted is that the temperature variations for Build 2 are very limited, which is consistent with the limited height of the sample and with the fact that aluminum alloys are known to be very good heat conductors. On the other hand, significant temperature increases are observed, especially from IR camera data. It should be first stated that what appears as a temperature band at the whole fabrication scale is an oscillation between high and low temperature corresponding to the laser on and off phases when considered at the layer scale, as shown in the insets of Figs. 9 and 10. This has already been observed by other authors (Marion *et al.*, 2014). For Build 1A, the averaged temperature on the sample surface recorded by using the thermal camera is shown in Fig. 9(a), which appears to oscillate between high and lower values. The maximum temperatures increase from 210 to 490 °C, while the lower temperatures increase from 50 to 350 °C.

The insets of Fig. 9 shows that the thermal camera signal increases sharply when the laser is in operation and decreases in-between melting/solidification cycles, as soon as the laser is switched off. The two discontinuities appearing periodically in the cooling phases are due to the recoater passage, which adds cooler powder on top of the warmer sintered part. For each fabrication cycle, the high values of the envelope correspond to the end of lasing, while the lower values are those recorded at the end of the cooling stage just prior to the resumption of the laser cycle. At a scale of a few layers, no drift is observable on both top and bottom signal values. Regarding the cooling characteristics, the averaged temperature on the sample surface is seen to recover its initial value over a time scale of a few seconds. Some calculations will be carried out in Sec. III D.

For Build 1B, the trends are qualitatively similar, but display significant differences in quantitative terms with the maximum temperatures increasing from 250 to 450 °C, while the lower temperatures increase from 50 to 250 °C. As mentioned earlier, the absolute temperature values from an IR camera should be taken with caution, but it can still be stated that the observed increases are clearly significant. Significant variation, albeit of a much more reduced range, is also observed from the TC data from below the fabrication plate in Fig. 10. Interestingly, a maximum is observed on the data for Build 1A, whereas a plateau is reached for Build 1B. As for Build 2, the variations also seem to reach a plateau, but what is more important is that they are again very limited in range.

Let us notice that TC data presented in Fig. 10 were also acquired; they will not be discussed here, as they only bring limited additional information, exhibiting a similar increase and decrease to the initial value observed for the IR data. The only significant difference is that the TC maxima, shown in the insets of Fig. 10, are not in phase with the end of the laser on phase, which can be qualitatively understood from the time lag necessary for heat propagation within the growing cylinders and the fabrication plate. To support this last assumption, it should be noted that the phase shift is much lower in Build 2 due to both smaller dimensions and faster heat diffusivity in aluminum alloys.

The question we now have to come back on is whether the measured temperature increases are consistent with the quasi-linear behavior for the TOF data shown in Fig. 7. The answer is quite simple for Build 2; with temperature increases way below 50 °C, the velocity variations deduced from Eq. (3) should remain much smaller than the 100 m/s uncertainty range. The situation is *a priori* less obvious for Builds 1A and 1B, and specially 1A for Build 1A where the temperature increases seem quite important. Indeed, the average sample temperatures (somewhat arbitrarily taken as the arithmetic mean of the IR and TC data) are expected to evolve from roughly 100 °C at the beginning of fabrication to circa 250 °C at the end of the process. Nevertheless, taking into account the temperature coefficient of Eq. (2a), such a 150 °C variation would result in a 72 m/s velocity difference, thus again within the 100 m/s uncertainty range. Applying the same procedure for Build 1B, we find that the average sample temperatures rise from roughly 100 °C at the beginning of fabrication to circa 200 °C at the end of the process. Applying the temperature coefficient of Eq. (2b), such a 100 °C variation would result in a 66 m/s velocity difference, thus again within the 100 m/s uncertainty range.

In such a context, it can thus be concluded that the linearity of the TOF variation at the fabrication scale is not inconsistent with the temperature variations measured from IR and TC data. However, the temperature information extracted from the TOF variation at the fabrication scale in Sec. III A should be taken with care, especially on quantitative grounds in view of the relatively large error bars on velocity measurements. On the other hand, our opinion is that on special events, such as the end of fabrication shown in Fig. 8, a variation of the TOF signal be significantly related to a temperature difference. As such, the comparison between the temperatures at the

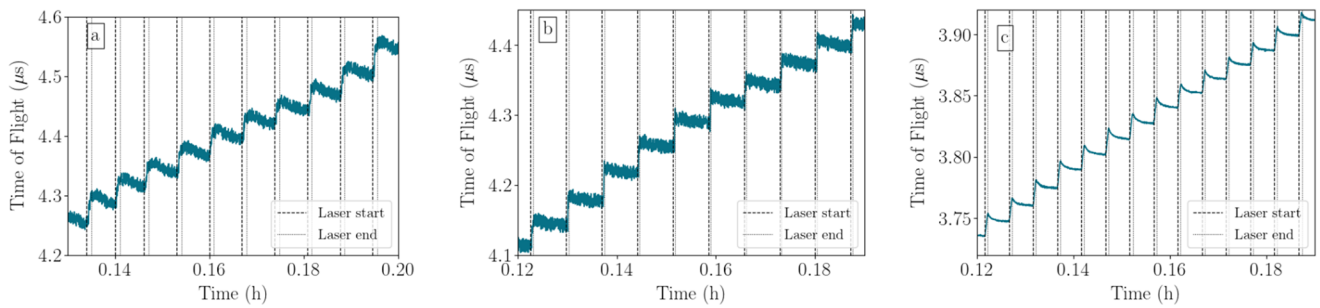


FIG. 11. TOF data at the beginning of fabrication for Builds (a) 1A, (b) 1B, and (c) 2.

end of fabrication taken on the one hand from IR and TC data and from the TOF relaxation on the other (respectively, 250 °C vs 268 °C for Build 1A and 200 °C vs 134 °C for Build 1B) can be considered to be in good order of magnitude agreement.

To sum things up before turning to the analysis of the data at the layer scale, our opinion is that even though the analysis of the time of flight data at the scale of the whole sample is limited by the relatively high uncertainty on velocity measurements, its processing may provide useful information in terms of process control. For instance, potential deviations from the linearity of the time of flight could be taken as warning signals regarding the porosity of the fabricated samples, or the study of the relaxation observed at the end of the fabrication could be used to check that the heat accumulation within the sample during the whole process remains between acceptable bounds.

C. Time of flight data at build layer scale and detection of a variation in process parameters

Shown in Fig. 11 are the TOF variations over a few cycles in the early stages of fabrication for Builds 1A (a), 1B (b) and (2) (c), corresponding to the IR camera and thermocouples signals in insets of Figs. 9 and 10. For each cycle, the beginning (respectively, the end) of the lasing phase is marked with a dashed (respectively, dotted) line. A first point worth noticing in Fig. 11 is that the signal quality is much better in Build 2 due to the increase of the sampling and pulse

repetition frequencies and due to the implementation of a moving average procedure that significantly improves the signal/noise ratio. Nonetheless, the signals are qualitatively similar, with an increase of the TOF during each lasing phase, followed by a decrease until the beginning of the next lasing phase. After each lasing phase, the signals do not recover the value they had before the laser was turned on, which can be related to the fact that matter has been added to the growing cylinder, thus increasing the length of the US path. Therefore, it can be stated that the TOF increase is due to both a temperature increase during lasing and the addition of matter. When considered at the whole fabrication scale, in Fig. 7, such a staircase evolution is not visible, and only the effect of matter addition can be observed.

The decrease when the laser is off is due to a cooling of the whole part. Indeed, during these periods, the last layer added is solidified, so the cylinder height is constant. The thermal dilatation does not have a significant effect at these times, issue that we deliberately put aside until now, but that needs to be addressed is that of thermal dilatation. Indeed, it can be thought that the significant temperature increases observed during the fabrications could have a significant impact on the length to be probed by the ultrasonic wave and thus conclusions drawn. However, taking an upper limit of the average linear expansion coefficient for Inconel 625 of $15 \times 10^{-6} \text{ K}^{-1}$, the relative length increase remains below 0.4% even at a maximum average temperature of 250 °C and thus way below what can be detected from our measurement device. For Build 2, as

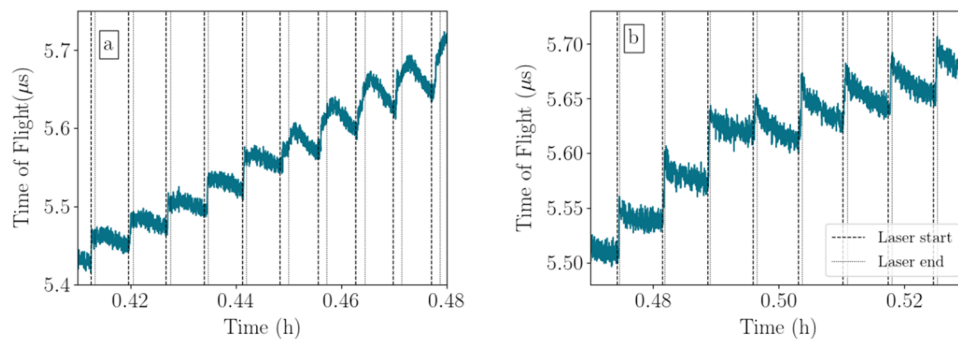


FIG. 12. Time of flight scan at the instant of scan velocity modification from 2000 to 900 mm/s for (a) Build 1A and (b) Build 1B.

the temperature increases are much smaller, the dilatation effect can even be more safely neglected. Residual stresses that generated thermal gradients (Machirori *et al.*, 2021) could also affect the time of flight during cooling phases.

An interesting result is observed during Builds 1A and 1B, when the manufacturing of the skirt is finished, and the cylinder begins to be built. From the 65th layer, laser power and scanning speed are modified, resulting in longer lasing times and greater heat input for each fusion cycle, as illustrated in Fig. 12. Subsequently, the increase in flight time during melting cycles is greater, and faster cooling kinetics are observed. This result is confirmed by the data recorded by using the IR camera at this time, shown in Fig. 13, and by thermocouples, with temperature increasing in Fig. 10 at ~30 min into the manufacturing process for Builds 1A and 1B.

For these builds, the temperature under substrate increases after the process parameters modifications, and the cooling kinetics at the top of the cylinders are slower, indicating a greater heat input for each melting cycle. Thus, the time of flight measurement is able to detect a variation of the process parameters and could be used in monitoring the LPBF process in real time.

D. Toward a cooling kinetics study and discussion

One of the purposes of the present section is to show that significant information can be retrieved from the cooling kinetics of time of flight after the laser has been turned off. More precisely, the characteristic cooling times can be derived using the ratio of the variation amplitude to the signal derivative at the beginning of the “laser off” phase. In technical terms, the derivative is estimated by a fit on the first three points of the cooling period. Such a procedure could probably be optimized, especially with the objective to reduce the dispersion, but it will be shown to be sufficient at this point for a proof of concept of the potential of the technique. Such a procedure would yield a well-defined argument if the signal was a decaying exponential, but it provides in all cases a characteristic time useful for order of magnitude purposes.

When applied to Builds 1A and 1B where no significant deviation with a linear trend can be inferred on the observed signals, in part due to the limited signal-to-noise ratio, the procedure yields a

characteristic time that is equal to the duration of the cooling phase, respectively, of 20 and 24 s for Builds 1A and 1B. On the other hand, exponential-like signals observed on the time of flight data for Build 2 allow for identifying a characteristic cooling time varying between 4 and 6 s. We will now turn to the analysis of the IR data to show that these characteristic cooling times bring some insights into the heat transfer phenomena along fabrication.

More precisely, when applying the characteristic time extraction procedure proposed for the TOF data on Build 2, the values for the signals in insets of Fig. 9 are, respectively, 2.5, 1.8, and 0.7 s for Builds 1A, 1B, and 2, respectively.

While it is unfortunately not possible to quantitatively compare IR and TOF data for Builds 1A and 1B due to an insufficient quality of the TOF signals, it can be stated that the characteristic decay times for the IR data are much smaller compared to those from TOF data. Regarding Build 2, where a quantitative comparison is possible due to a much better TOF signal quality, the results for the whole fabrication, where a 15 points moving average procedure has been applied, are shown in Fig. 14. Even though the data are quite noisy, it appears clearly that the characteristics decay time from TOF data is again significantly higher compared to those from IR data. As the time of flight is sensitive to the temperature field all along the ultrasound

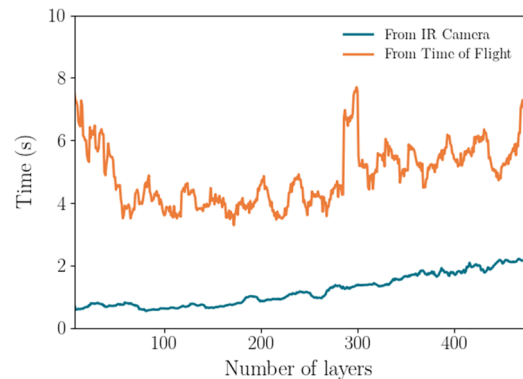


FIG. 14. Characteristic cooling times in Build 2 from thermal camera and ultrasonic time of flight.

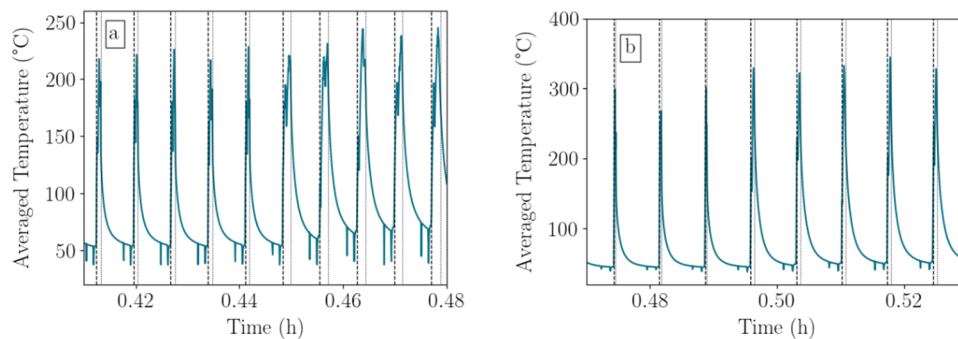


FIG. 13. Temperatures from the IR camera at the moment of scan velocity modification of 2000 to 900 mm/s for (a) Build 1A and (b) Build 1B.

propagation path, one can expect a longer equilibration duration compared to the thermal camera that only probes the sample top surface. Another way of expressing this is to say that the characteristic cooling time of a body depends on its thermal mass, a larger thermal capacity implying a longer cooling time. Thus, the difference between TOF and IR data can be qualitatively understood as the difference in cooling times between a small region of a few layers and that of the full cylinder-fabrication plate system as sensed by the ultrasound measurement.

To extend this qualitative discussion about cooling kinetics, we believe that our experimental data could be used profitably to validate a numerical model of the heat transfer phenomena within the fabricated part. Such a numerical model would probably have to include several things to be realistic: a layer scale time discretization, a heat conduction model taking into account the plate material, the cylinder properties, as well as overall heat transfer coefficients for convection and radiation. The implementation of such a model is outside the scope of the present work. Nevertheless, it can be expected that the qualitative discussion of the heat transfer phenomena proposed herein should help in guiding the formulation of the model as well as the numerical estimation of the associated parameters.

IV. CONCLUSION

The objective of the present work was to propose a proof of concept of the ability of ultrasound time of flight measurements to complement existing temperature measurements in a laser powder bed fusion additive manufacturing process. To this end, two different printers (a 3D Systems ProX DMP 320 and a Farsoon FS271M) were instrumented, with ultrasonic transducers located underneath specialized fabrication plates below the parts to be probed. Thermocouples were installed near the transducers, and thermal cameras able to monitor the part top surface temperature were also included. Three cylinder parts among those fabricated were discussed here, two on the 3D Systems ProX DMP 320 printer with an Inconel 625 alloy and one on the Farsoon FS271M printer with an aluminum AlSi7Mg0.6 alloy.

From an experimental standpoint, the first thing to be stated is that we managed to measure *in situ* time of flight signals, which allowed us to obtain a wealth of relevant information at both the macroscopic (i.e., whole fabrication) and the microscopic (i.e., single build cycle) scales. For instance, the variation of the time of flights after the end of fabrication was meaningfully related to a decrease of the average temperature of the samples. At the layer scale, a significant observation is that the characteristic cooling times measured on the time of flight signal were in all cases much longer than those measured by using the surface camera. Such findings support the validity of the ultrasound technique to probe the whole length of the fabricated part and thus of its ability to provide complementary information as compared to say a thermal camera, which only measures the temperature at the top of the fabricated sample.

This study lays the foundations for the use of ultrasound, and in particular of ultrasonic time of flight measurement, for *in situ* monitoring of the LPBF process, and shows a real potential. Such a measurement could lead to process monitoring, to ensure that there are no defects in the running of the process, but also to real-time monitoring of the temperature field, through the development

of a thermal model, and an inverse problem. An ultrasonic time of flight measurement can be used to calculate the wave velocity in the sample, which can provide information on its microstructure, or potential defects, as shown by Rieder *et al.* (2014; 2016). *In situ* monitoring of melting pool behavior can also be envisaged, for which several studies have already been carried out off-machine (Yang *et al.*, 2021). However, it should also be stated that we were not fully satisfied with the quality of the *in situ* ultrasound signals. As stated in the text, only one echo reflected on the top of the cylinder was unambiguously determined, which is a situation usually avoided when measuring ultrasonic time of flights since it introduces bias due to the coupling medium. In addition, the relatively limited signal-to-noise ratio can also be due to an inefficient transmission of ultrasonic waves in the plate and the cylinder. Indeed, some uncertainties were identified regarding the couplant used because the signal quality degrades over time and accordingly, to temperature. In addition, the procedure for couplant application remains empirical.

In this respect, a first obvious perspective of the present work would be to work on the improvement of signal quality. For instance, procedures allowing for an accurate alignment of the transducer with the cylinder should be explored in order to reduce interferences, whether internal to the cylinder or with the fabrication plate, and thus allow us to significantly increase the signal-to-noise ratio of the acquired data. Similarly, the identification of a couplant able to withstand the harsh machine environment, and an automated application procedure, would also be a clear advantage in order to improve the ultrasonic signal quality.

Another perspective of the present work would be to use our experimental data for the validation of a numerical model of the heat transfer phenomena within the fabricated part. Such an approach would allow going much deeper into the physics of the problem, as compared to the qualitative explanations proposed in this paper. Since our data are acquired at the layer scale, such a thermal model would need to be formulated at the same scale. However, even assuming the use of overall heat transfer coefficients for convection and radiation, the choice of relevant phenomena to be accounted for is not *a priori* obvious. Nevertheless, it can be expected that the qualitative discussion of the heat transfer phenomena proposed herein can help in guiding the formulation of the model.

ACKNOWLEDGMENTS

The authors would like to thank Additive Factory Hub platform colleagues Pierre Lapouge, Socona Traoré, and Corinne Dupuy and CEA LITEN colleagues Michel Pellat and Guilhem Roux for their much-appreciated help in setting up the experiments, respectively, on the 3D Systems ProX DMP 320 printer and on the Farsoon FS271M printer.

AUTHOR DECLARATIONS

Conflict of Interest

The authors have no conflicts to disclose.

Author Contributions

M. Palla: Formal analysis (equal); Investigation (equal); Methodology (equal); Software (equal); Validation (equal); Visualization (equal); Writing – original draft (equal); Writing – review & editing

(equal). **F. Le Bourdais**: Conceptualization (equal); Funding acquisition (equal); Methodology (equal); Software (equal); Supervision (equal); Writing – review & editing (equal). **J. P. Garandet**: Conceptualization (equal); Funding acquisition (supporting); Methodology (equal); Supervision (lead); Writing – review & editing (equal).

DATA AVAILABILITY

The raw/processed data can be made available upon reasonable request. The raw/processed data required to reproduce these findings cannot be shared openly at this time as the data also form part of an ongoing study.

REFERENCES

- Bartlett, J. L., Heim, F. M., Murty, Y. V., and Li, X., “*In situ* defect detection in selective laser melting via full-field infrared thermography,” *Addit. Manuf.* **24**, 595–605 (2018).
- Boucher, R. and Hassab, J., “Analysis of discrete implementation of generalized cross correlator,” *IEEE Trans. Acoust., Speech, Signal Process.* **29**(3), 609–611 (1981).
- Carter, G. C., “Time delay estimation,” in *Adaptive Methods in Underwater Acoustics*, edited by H. G. Urban (Springer Netherlands, 1985), pp. 175–196.
- Chen, T.-F., Nguyen, K. T., Wen, S.-S. L., and Jen, C.-K., “Temperature measurement of polymer extrusion by ultrasonic techniques,” *Meas. Sci. Technol.* **10**(3), 139 (1999).
- DebRoy, T., Wei, H. L., Zuback, J. S., Mukherjee, T., Elmer, J. W., Milewski, J. O., Beese, A. M., Wilson-Heid, A., De, A., and Zhang, W., “Additive manufacturing of metallic components—Process, structure and properties,” *Prog. Mater. Sci.* **92**, 112–224 (2018).
- Gawel, T., “Review of additive manufacturing methods,” *Solid State Phenom.* **308**, 1–20 (2020).
- Giannatsis, J. and Dedoussis, V., “Additive fabrication technologies applied to medicine and health care: A review,” *Int. J. Adv. Des. Manuf. Technol.* **40**(1–2), 116–127 (2009).
- Ihara, I., Tomomatsu, T., Takahashi, M., Kosugi, A., Matsuya, I., and Yamada, H., “Ultrasonic thermometry for temperature profiling of heated materials,” in *Advancement in Sensing Technology: New Developments and Practical Applications*, edited by Mukhopadhyay, S. C., Jayasundera, K. P., and Fuchs, A. (Springer, 2013), pp. 211–236.
- Javidrad, H. R. and Salemi, S., “Determination of elastic constants of additive manufactured Inconel 625 specimens using an ultrasonic technique,” *Int. J. Adv. Des. Manuf. Technol.* **107**(11), 4597–4607 (2020).
- Kouprianoff, D., Yadroitsava, I., du Plessis, A., Luwes, N., and Yadroitsev, I., “Monitoring of laser powder bed fusion by acoustic emission: Investigation of single tracks and layers,” *Front. Mech. Eng.* **7**, 678076 (2021).
- Kumar, A., Shankar, V., Jayakumar, T., Rao, K. B. S., and Raj, B., “Correlation of microstructure and mechanical properties with ultrasonic velocity in the Ni-based superalloy Inconel 625,” *Philos. Mag. A* **82**(13), 2529–2545 (2002).
- Lerner, A., Pouille, Q., Ladaci, A., Cotillard, R., Lomello, F., Aubry, P., Maskrot, H., Bouwmans G., and Laffont G., “Selective laser melting *in situ* temperature monitoring using femtosecond point-by-point fiber Bragg gratings,” in 27th International Conference on Optical Fiber Sensors (2022), Paper W4.8, 2022.
- Liang, H., Yang, F., Yang, L., Liu, Z., Wang, G., Wei, Y., and Xue, H., “Research and implementation of a 1800 °C sapphire ultrasonic thermometer,” *J. Sens.* **2017**, 1–7.
- Machirori, T., Liu, F. Q., Yin, Q. Y., and Wei, H. L., “Spatiotemporal variations of residual stresses during multi-track and multi-layer deposition for laser powder bed fusion of Ti-6Al-4V,” *Comput. Mater. Sci.* **195**, 110462 (2021).
- Marion, G., Cailletaud, G., Colin, C., and Mazière, M., “A finite element model for the simulation of direct metal deposition,” in *International Congress on Applications of Lasers and Electro-Optics* (ASME, 2014), pp. 834–841.
- Mitchell, J. A., Ivanoff, T. A., Dagle, D., Madison, J. D., and Jared, B., “Linking pyrometry to porosity in additively manufactured metals,” *Addit. Manuf.* **31**, 100946 (2020).
- Nadimpalli, V. K., “Ultrasonic nondestructive evaluation of metal additive manufacturing,” Ph.D. thesis, University of Louisville, 2018, <https://ir.library.louisville.edu/etd/2901>.
- Palla, M., “Caractérisation par ultrasons du champ de température dans un procédé de fabrication additive du type powder bed fusion,” Ph.D. thesis, Université Grenoble Alpes, 2023, <https://www.theses.fr/2023GRALI087>.
- Raffestin, M., Domashenkov, A., Bertrand, P., Faverjon, P., and Courbon, C., “Ultrasonic diagnostic for in situ control in metal additive manufacturing,” *Measurement* **206**, 112244 (2023).
- Rieder, H., Dillhoefer, A., Spies, M., Bamberg, J., and Hess, T., “Online monitoring of additive manufacturing processes using ultrasound,” in ECNDT 2014, 2014.
- Rieder, H., Spies, M., Bamberg, J., and Henkel, B., “On- and offline ultrasonic characterization of components built by SLM additive manufacturing,” *AIP Conf. Proc.* **1706**, 130002 (2016).
- Shi, Y.-A., Wei, D., Hu, B., Zeng, L., Du, Y.-X., and Gui, Y.-W., “A method for reconstructing internal temperature distribution in solid structure,” *J. Nondestr. Eval.* **39**, 48 (2020).
- Slotwinski, J. A., Garboczi, E. J., and Hebenstreit, K. M., “Porosity measurements and analysis for metal additive manufacturing process control,” *J. Res. Natl. Inst. Stand. Technol.* **119**, 494 (2014).
- Svilainis, L., “Review of high resolution time of flight estimation techniques for ultrasonic signals,” in 52nd Annual Conference of the British Institute of Non-Destructive Testing 2013, NDT 2013, 2013.
- Svilainis, L., “Review on time delay estimate subsample interpolation in frequency domain,” *IEEE Trans. Ultrason. Ferroelectrics Freq. Control* **66**(11), 1691–1698 (2019).
- Uriondo, A., Esperon-Miguez, M., and Perinpanayagam, S., “The present and future of additive manufacturing in the aerospace sector: A review of important aspects,” *Proc. Inst. Mech. Eng., Part G* **229**(11), 2132–2147 (2015).
- Wadley, H. N. G., Norton, S. J., Mauer, F., and Droney, B., “Ultrasonic measurement of internal temperature distribution,” *Philos. Trans. R. Soc. London, Ser. A* **320**(1554), 341–361 (1986).
- Wang, Y., Zou, F., and Cegla, F. B., “Acoustic waveguides: An attractive alternative for accurate and robust contact thermometry,” *Sens. Actuators, A* **270**, 84–88 (2018).
- Yan, Z., Liu, W., Tang, Z., Liu, X., Zhang, N., Li, M., and Zhang, H., “Review on thermal analysis in laser-based additive manufacturing,” *Opt. Laser. Technol.* **106**, 427–441 (2018).
- Yang, T., Jin, Y., Squires, B., Choi, T.-Y., Dahotre, N. B., and Neogi, A., “In-situ monitoring and ex-situ elasticity mapping of laser induced metal melting pool using ultrasound: Numerical and experimental approaches,” *J. Manuf. Process.* **71**, 178–186 (2021).